Slip distributions on intersecting normal faults

Laurent Maerten [a, *], Emanuel J. M. Willemse [a, 1], David D. Pollard [a], Keith Rawnsley [b]

[a]*The Rock Fracture Project, Stanford University, Stanford, CA 94305-2115, USA*
[b]*Elf Aquitaine Production, CSTJF avenue Larribau, 64018 Pau Cedex, France*

Abstract

Slip distributions on normal faults often are asymmetric and display multiple local maxima. Numerically computed slip distributions from elastic models indicate that such irregular slip distributions can be caused by mechanical interaction between intersecting faults that produce local perturbations of the stress field resolved on the faults.

A three-dimensional boundary element model based on the displacement discontinuity method has been used to analyze the mechanical interaction of faults that form Y- or T-shaped intersections. Slip distributions are asymmetric with a steeper slip gradient toward the line of intersection. Multiple slip maxima occur, depending on the angle between the faults, but generally they are not located along the intersections, nor at the fault centers.

Examples of intersecting normal faults taken from oil reservoir seismic surveys and sandbox experiments have been used to confirm the application of the theoretical results. Despite considerable simplifications in terms of geometry and boundary conditions, the computed slip distributions capture the characteristics of the observed slip distributions. © 1999 Elsevier Science Ltd. All rights reserved.

1. Introduction

Simple normal faults have been idealized with elliptical tip lines and slip distributions that are symmetrical about a single and central slip maximum (Rippon, 1985; Watterson, 1986; Barnett et al., 1987; Walsh and Watterson, 1989). Theoretical models of a single fault in an isotropic and homogeneous elastic material subjected to a uniform remote shear stress and a lesser uniform shear traction on the fault surfaces have an elliptical variation in slip (Sih, 1975; Tada et al., 1985). However, research over the past several years has shown that fault slip distributions are unlikely to be symmetrical. For instance, Peacock and Sanderson (1991, 1994) and Childs et al. (1995) describe a steepening of the slip distribution and positioning of the maximum slip toward the relay zones of overlapping faults. Bürgmann et al. (1994), Peacock and Sanderson (1996), Willemse et al. (1996) and Willemse (1997) discuss the slip distribution on two overstepping fault segments and show that mechanical interaction between the segments can lead to asymmetric slip distributions. Slip distributions that exhibit multiple slip maxima near the line of intersection between two faults have been documented by Walsh and Watterson (1991), Childs et al. (1993), Needham et al. (1996) and Nicol et al. (1996). These slip maxima are usually associated with local zones of high slip gradients, often several times greater than typical slip gradients over the rest of the fault surface.

There are many linked fault geometries that provide commonly observed deviations from the ideal single elliptical fault with zero slip at the tip line and maximum slip at the center (Rippon, 1985; Watterson, 1986; Barnett et al., 1987; Walsh and Watterson, 1989). For example, segmented normal faults can merge and form a single through-going fault with synthetic splays (Childs et al., 1993, 1995), developing a

---

* Corresponding author. E-mail: laurent@pangea.stanford.edu.
[1] Now at Shell International Exploration and Production, Rijswijk, Netherlands.
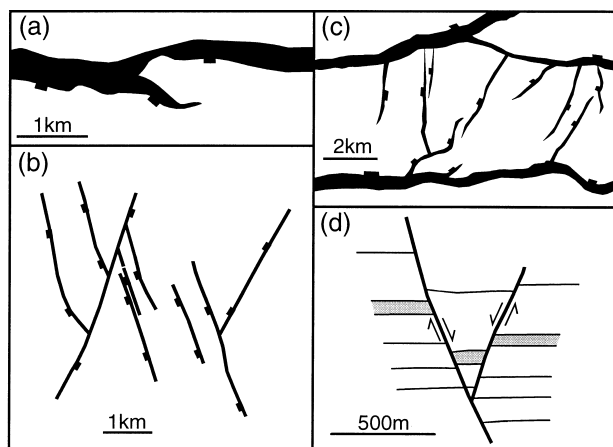
Fig. 1. Typical linked fault geometries. (a) Map view of a normal fault and its synthetic splay from the northern North Sea forming a 'Y' intersection (modified from Childs et al., 1995). (b) Map view of the Chimney Rock orthorhombic fault array (Utah) forming 'Y' intersections (modified from Krantz, 1988). (c) Map view of two normal fault sets that link together to form 'T' or 'Y' intersections, from the Norwegian part of the North Sea (courtesy of Norsk Hydro). (d) Cross-section of a 'conjugate' fault system from the Timor Sea (modified from Nicol et al., 1996).

Y-shaped geometry in map view (Fig. 1a). Normal faults produced during a single tectonic phase can be grouped into different fault sets in map view. For instance, the fault sets can have an orthorhombic geometry (Fig. 1b) in response to a three-dimensional strain and produce Y-shaped patterns (Aydin and Reches, 1982; Reches, 1987; Krantz, 1988). Normal fault patterns can be composed of T- or Y-shaped traces (Fig. 1c) when the main faults are a direct product of, and strike roughly perpendicular to, the direction of regional extension, whereas the smaller faults, striking at angles less than 90° to the direction of extension, are contemporaneous adjustment faults (Fossen and Rørnes, 1996). In cross-section, extension can be accommodated by antithetic faults (Anderson, 1951) that compose 'conjugate' systems (Fig. 1d).

In this paper, we examine slip distributions on intersecting normal faults and describe their systematics. The purpose is to provide, via mechanical modeling and field observation, insights into the effect of the 'T', 'Y', and conjugate geometries on slip distributions. We use the component of slip in the dip direction (dip-slip) as the physical quantity to characterize normal faults. This also facilitates the comparison with natural examples from seismic reflection surveys where the strike-slip motions are seldom measured. The distribution of dip-slip provides a quantitative assessment of the extent of mechanical interaction among the faults. We use mechanical models to investigate complex normal faults as observed in reflection seismic surveys and a sandbox experiment. The models, together with geologically reasonable boundary conditions, are used to compute slip distributions, which are then compared with the observed slip so theoretical models can be calibrated (Oreskes et al., 1994).

The conclusions are derived from idealized numerical models in terms of geometry, material properties, and boundary conditions. Nonetheless, they suggest that mechanical interaction between intersecting faults can strongly perturb slip distributions. Understanding this behavior not only provides insight into the mechanics of intersecting faults, but could eventually help to develop methods to refine seismic interpretation and predict fault linkage as described by Maerten (1998).

2. Numerical analysis

2.1. Boundary element method

The investigation of perturbed fault-slip distributions, as caused by the interaction between faults with complex three-dimensional geometries, has been performed using Poly3D, a three-dimensional boundary element program (Thomas, 1993). Poly3D is based on the displacement discontinuity method and the governing equations of linear elasticity theory (Crouch and Starfield, 1983; Becker, 1992). Poly3D uses the solution for an angular dislocation in a linear elastic half space (Comminou and Dunders, 1975) and superimposes several angular dislocations to form a polygonal dislocation surface (Jeyakumaran et al., 1992). Multiple polygonal dislocation surfaces are joined together to form faults with complex geometries.

Mechanical interaction is modeled by prescribing traction boundary conditions at the center of each polygonal element comprising the faults. The two in-plane shear tractions and the normal traction on each element can be prescribed as a boundary condition either directly on the element centers or by remotely applied stresses. Alternatively, the uniform components of the displacement discontinuity over the entire element can be prescribed. The behavior of the linear elastic and isotropic solid is characterized by two elastic constants, Poisson's ratio and the shear modulus. We took a value of 0.25 for Poisson's ratio and 15 000 MPa for the shear modulus, which are representative of many rocks (Clark, 1966). In all the models presented here, the displacement discontinuity perpendicular to the fault was prescribed to be zero, thereby preventing opening or interpenetrating of the fault walls. Otherwise, the fault surfaces are allowed to accommodate the appropriate dip-slip or strike-slip motion that would result from prescribed shear tractions and remote stress state.

2.2. Model assumptions

The models only address fault interaction through perturbation of the shear stresses acting on the fault surfaces. Thus, changes in frictional resistance due to increases or decreases of normal stresses acting on the fault surfaces are not taken into account. Such normal stress changes are expected to be significant at contractional or extensional relay zones, so the results should be used with caution in such locations.

The models capture the mechanics of an idealized single slip event or a series of events that do not include any stress relaxation. Viscoelastic constitutive properties that would account for stress relaxation during accumulation of slip in a series of events are not considered (Rundle, 1982; Cohen, 1984; Fernandez et al., 1996).

The models, based on linear elasticity theory, produce a singularity in stress at the tip of the fault along with large slip gradients. These slip gradients contrast with more tapered slip distributions usually observed near the tip of natural faults. Several explanations for tapered slip distributions have been discussed in the literature: (1) integration of many elliptical slip distributions in which each slip event involves fault propagation (Walsh and Watterson, 1987, 1988); (2) inelastic deformation at the fault tip during fault growth (Cowie and Scholz, 1992; Cowie and Shipton, 1998); and (3) an increase in fault strength toward the fault tip to produce a cohesive end zone (Bürgmann et al., 1994; Willemse, 1997). In the models presented here the uniform fault shear strength and uniform remote stress results in large slip gradients near the tip line, and the faults do not propagate in response to these applied stresses. Furthermore, inelastic deformation as well as cohesive zones are not taken into account. Such considerations are very important for analysis of near-tip slip and secondary deformation, but are of little consequence for the distribution of slip over the majority of the fault. Therefore, no attempt is made to correct the slip distribution in the model fault tip region, and we focus attention on deviation from symmetrical slip distributions with maxima at the fault centers.

Given these limitations, we nonetheless show that simple elastic models capture some of the principal effects of fault mechanical interaction and illustrate the accompanying slip perturbations.

3. T- or Y-shaped normal faults

3.1. Model configurations

To understand the resulting slip distributions on typical three-dimensional normal fault arrays, we in-

vestigate the behavior of the Y- or T-shaped intersection of two normal faults with different strikes. The model configuration consists of two normal faults dipping at 60°. Fault A has an elliptical tip line with an aspect ratio of 2, the horizontal length being twice the fault dip dimension which has a unit value (Fig. 2). Fault B has the same tip line shape but it is truncated by fault A. The aspect ratio of 2 is approximately equal to the average aspect ratio observed in some normal fault data sets that vary between 1.25 and 3 (Rippon, 1985; Barnett et al., 1987; Walsh and Watterson, 1989; Nicol et al., 1996). The two faults are linked together at their centers. Because one of them truncates the other, they form the 'T' or 'Y' pattern. As both faults dip at 60°, the intersection line is oblique to the elliptical axes of fault A.

The two linked normal faults are modeled in a number of different configurations. By changing the strike of the faults, they form a 'T' or 'Y' geometry in plan view. The angle α is defined as the clockwise angle between the strike lines of the faults (Fig. 2). In the simulations, α varies from 30° to 180° with steps of 30°. The case $\alpha = 180°$ is treated as a single planar elliptical fault, which is used as a reference or base case.

Each fault has its own coordinate system, as shown in Fig. 2. The x^f-axis is directed down dip; the y^f-axis is directed along strike; and the z^f-axis is normal to
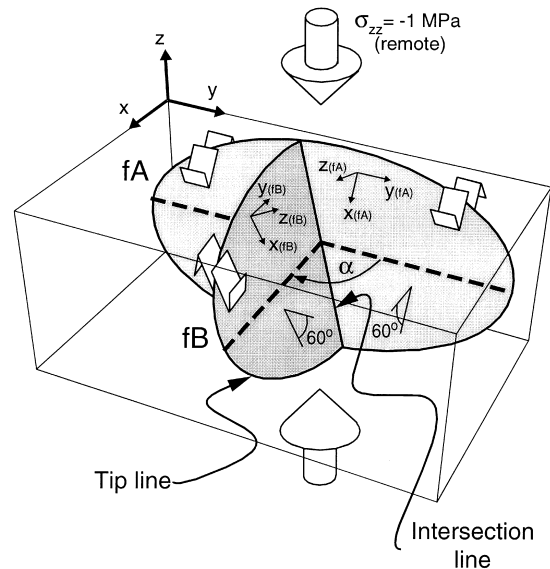

Fig. 2. The configuration of the theoretical models consists of two normal faults dipping 60°. Fault A has an elliptical tip line with an aspect ratio of 2 so that half the length (1 unit) is the fault dip-parallel dimension. Fault B has the same elliptical shape but it is truncated by fault A. The faults are linked together along their center to form an intersecting fault array. The angle α is the angle between the strike of the faults which, in our models, varies from 30° to 150° with steps of 30°. The big arrows represent the direction of applied vertical compressive stress ($\sigma_{zz} = -1$ MPa) and the dashed lines are the observation lines of Fig. 3(b).

the fault plane: a global coordinate system is used with the z-axis vertical.

The model material corresponds to a homogenous whole elastic space. This is representative of natural faults that are buried very deeply relative to their in-plane dimensions and where the free surface has insignificant effects. In order to produce the same tractions on the two fault surfaces we apply a remote homogeneous compression in the global z coordinate direction, $\sigma_{zz} = -1$ MPa. In the absence of slip on the faults, this produces a uniform extension in the x and y directions and shortening in the z direction:

$$\varepsilon_{xx} = \varepsilon_{yy} = -\frac{\nu \sigma_{zz}}{E} \quad \text{and} \quad \varepsilon_{zz} = \frac{\sigma_{zz}}{E}$$

where ν = Poisson's ratio and E = Young's modulus.

We use the conventions employed in engineering mechanics, e.g. the principal stresses are arranged such that $\sigma_1 > \sigma_2 > \sigma_3$, with tension positive.

3.2. Slip distribution and shear stress relationship

Fig. 3(a) shows the contours of the computed dip-slip over the two modeled faults for $\alpha = 90°$. Fault slip is normalized to the maximum slip that would occur if fault A were isolated. Fault A has two distinct slip maxima on either side of the intersection line. On the footwall side of fault B, the maximum dip-slip on fault A is reduced to about 80% of the base case maximum whereas, on the hanging wall side, it is increased to about 120%. In addition, mechanical interaction leads to an asymmetric slip distribution and a steep slip gradient near the intersection line. Fault B has a single
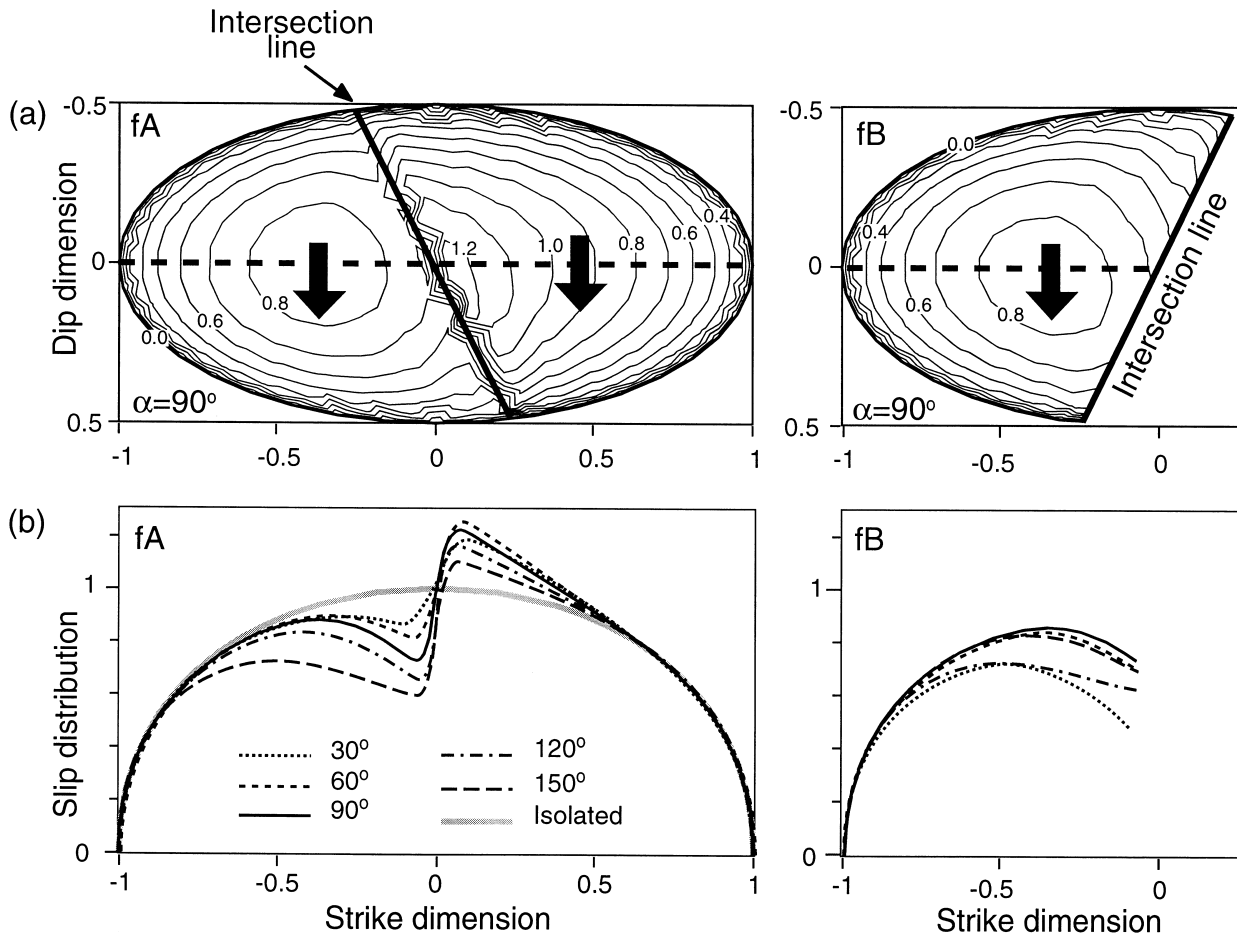

Fig. 3. Computed slip distributions for the theoretical models. (a) Contoured three-dimensional distribution of normalized vertical slip along the two dipping faults (case $\alpha = 90°$). The contour value of 1 indicates the maximum that would occur on a single isolated fault. Dashed horizontal lines are the position of (b). Black arrows show the sense of slip on the hanging wall of the faults. (b) Computed slip distribution on the faults along a horizontal line through their center for angle α varying from $30°$ to $150°$ with steps of $30°$. Black curves show computed slip for different α and the bold gray curve represents slip along a single isolated fault. Mechanical interaction leads to slip variations near the fault intersection.

asymmetric slip maximum that is about 80% of the base case.

Fig. 3(b) is a graph of the slip variation along a horizontal line at mid height of the faults for various angles α. The slip along the right half of fault A (the hanging wall side of fault B) is always greater than, or equal to, that of an isolated planar fault (bold gray line), whereas the slip on the left half of fault A (footwall side of fault B) is always less than or equal. With increasing angle α, the magnitude of the dip-slip maximum on the left half decreases, whereas that on the right half increases (from $\alpha = 30°$ to $\alpha = 60°$) then decreases (from $\alpha = 60°$ to $\alpha = 150°$). The asymmetry in the slip distribution on fault A occurs for all values of α considered.

The slip distribution on fault B (Fig. 3b) is more complicated and it was difficult to apply a simple rule to explain the slip variations related to varying α. This complication apparently is due to the change in shape of fault B as it is truncated by fault A for various values of α. The maximum slip remains adjacent to, but not at, the intersection line for all the configurations.

These model results can be explained in terms of perturbation of the stress components acting on the fault surfaces due to fault interaction (Bürgmann et al., 1994; Willemse et al., 1996; Willemse, 1997). Here the perturbation of normal stress is not considered, but it is instructive to understand how the faults interact by modifying the local shear stress field on their neighbor. Where the stress perturbation from slip on one fault increases the down dip shear stress on its neighbor, it will tend to enhance slip. Where the stress perturbation lowers the down dip shear stress, slip on the neighbor will tend to decrease.

In Fig. 4(a), we use the case $\alpha = 90°$ to illustrate the down dip shear stress on fault A caused by dip-slip on fault B. The shear stress $\sigma_{zx}(fA)$ caused by motion of fault B is contoured on an observation plane that coincides with fault A. The maximum shear stress perturbation is concentrated at the intersection line and has opposite signs on either side.

Fig. 4(b) shows contours of the dip-slip on fault A caused only by the perturbed shear stress field due to fault B. A positive shear stress induces a normal slip and a negative shear stress induces a reverse slip on fault A. The dip-slip on fault A is in the normal sense on the hanging wall side of fault B and in the reverse sense on the footwall side. This result shows a direct relationship between the perturbed shear stress field and the slip distribution (Fig. 3). The positive shear stress induces a normal sense of slip, so the normal dip-slip is increased on that part of fault A. Where the perturbed shear stress induces a reverse sense of slip, the normal dip-slip distribution is decreased.

4. Natural examples of slip distributions

4.1. North Sea example

The first example has been taken from the seismic data of a North Sea oil field located west of the Shetland Islands. It consists of two Devonian normal faults that form a 'Y' geometry (see Fig. 5). Both the dip-slip of the faults and the elevation changes shown on a structure contour map have been compared to the numerical models.

The major normal faults (those with maximum slip greater than 200 m) of this area were formed during the Devonian extension as a consequence of NW–SE collapse of the Caledonian orogen (Coward and Enfield, 1987; Enfield and Coward, 1987). The orientations of normal faults are apparently controlled by
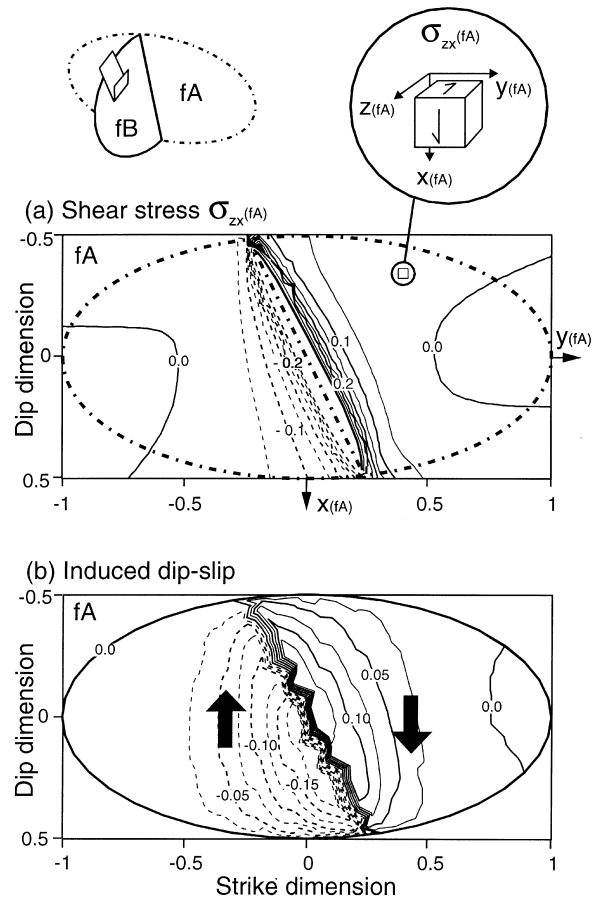

Fig. 4. Relationship between shear stress perturbation and slip variations for the theoretical models, $\alpha = 90°$. (a) Computed distribution of the fault-parallel shear stress $\sigma_{zx}(fA)$ caused by motion of fault B alone and contoured on an observation plane that coincides with fault A. Dashed contours are negative shear stress. (b) Contour of dip-slip distribution on a passive fault A caused by perturbed shear stress field due to slip on fault B. A positive shear stress induces a normal slip and a negative shear stress induces a reverse slip on fault A. Black arrows show the sense of slip on the hanging wall of the fault.

the grain of the basement (Brewer and Smythe, 1984; McClay et al., 1986). Most slip on the faults occurred during the Devonian extension, but there is evidence for reactivation during comparatively minor later tectonic events: (1) the NW–SE Cretaceous extension related to opening of the North Atlantic (Roberts et al., 1990); (2) the late Cretaceous and early Paleocene NNW–SSE contraction related to the Alpine orogeny; and (3) the NW–SE contraction inferred by Charpentier (unpublished Elf Aquitaine report, 1994) after the late Eocene subsidence. This contraction started during the early Miocene and continues to the present time.

The structure contour map shows two major normal faults that intersect, forming a Y-shaped pattern in map view (Fig. 5a). The slip distribution on the faults was obtained by measuring the offset structure contours (Fig. 5b and c) corrected by the dip of the faults. The uncertainty in the measured slip is about 25 m due to seismic resolution. There is abrupt reduction of slip along the N–S-trending through-going fault A where it is intersected by fault B. In addition, the point of maximum slip on the approximately E–W-trending fault B is located closer to the southern fault tip rather than at the line of intersection with fault A.

The geometry of the faults was simplified and idealized to planar surfaces with elliptical tip lines and the same down-dip height (Fig. 6). Based on seismic cross-sections, faults A and B dip 50° and 70°, respectively. In map view, the simplified model configuration approximates the geometry and length of the observed faults.

Three loading configurations have been used to analyze the effects of remote stress and a free surface: model (1) used a vertical compressive load in a whole space (Fig. 6a); model (2) used a horizontal tensile load in a whole space to simulate the NW–SE-trending Devonian extension (Fig. 6a); and model (3) used a horizontal tensile load in a half space to simulate the Devonian extension and the traction-free surface of the basin (Fig. 6b). For single isolated faults in a whole elastic space, these three different boundary conditions would lead to elliptical slip distributions. However, the slip distributions computed for models (1) and (2) are not elliptical because of the complex interaction between the fault segments. For model (3) further asymmetry is introduced by the free surface.

To facilitate comparison with the observed slip distribution, the computed slip has been normalized against the maximum slip observed in the example
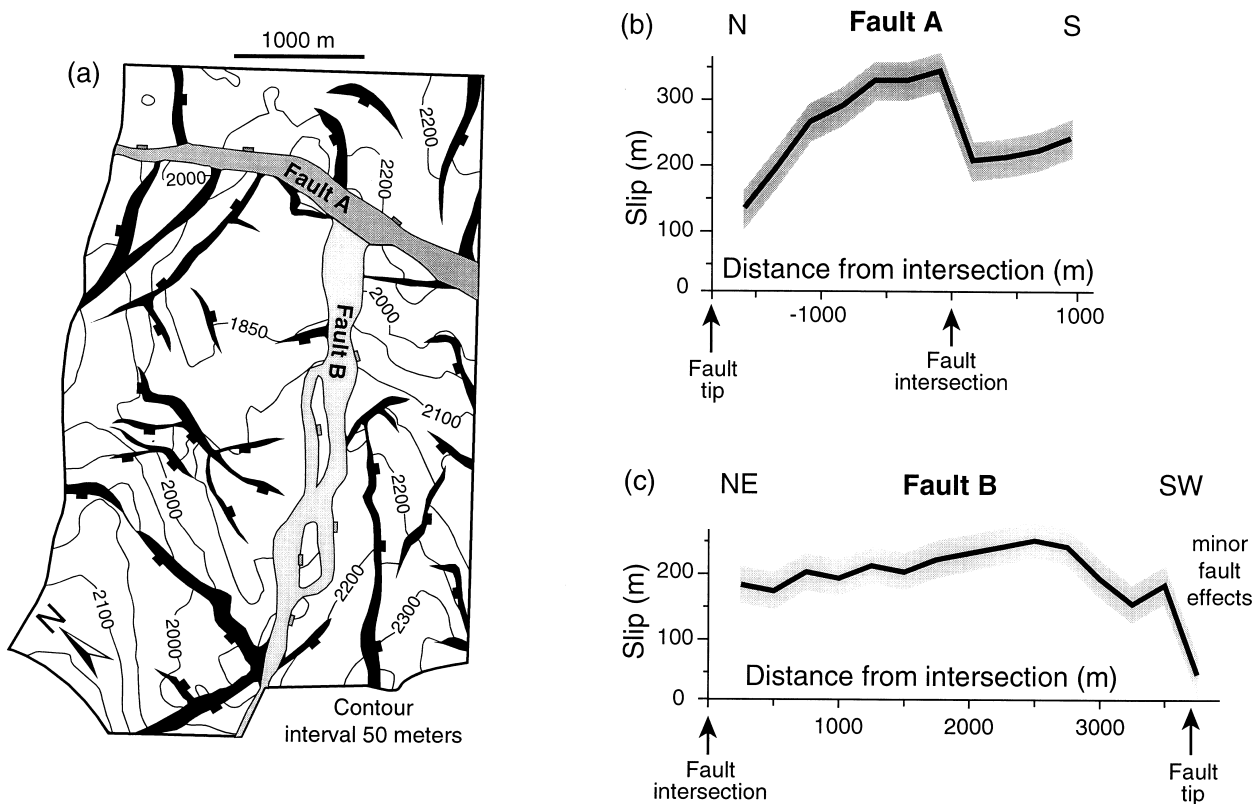

Fig. 5. Intersecting normal faults from an oil reservoir in the North Sea. (a) Structure contour map showing footwall uplift and hanging wall subsidence around two intersecting normal faults. (b) Measured slip distributions along fault A showing high slip gradient at the intersection with fault B. (c) Measured slip distributions along fault B showing slip maximum away from the intersection with fault A. Proximity of minor faults might cause local slip variation as observed on the SW tip of fault B. Shaded areas are the uncertainties in the measured slip.
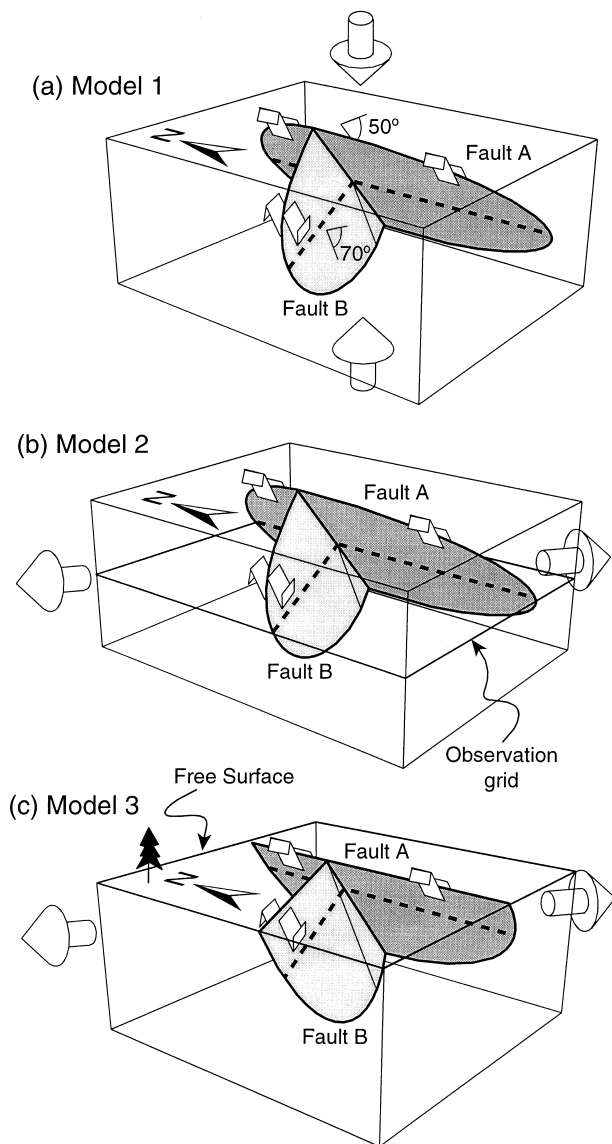
Fig. 6. Idealized fault geometries used to model the North Sea example. Faults A and B have been idealized by planar surfaces with length and dip angles obtained from seismic data. Dashed lines are observation lines through the center of the modeled faults. Three different model configurations have been considered to compute the slip distribution on faults A and B and to compare with observed slip. (a) Model 1 has been loaded with a vertical remote compressive stress (−1 MPa). (b) Model 2 has been loaded with a horizontal remote tensile stress (1 MPa) to simulate the direction of regional extension contemporaneous to faulting. (c) Model 3 has been loaded with the same horizontal remote tensile stress associated with a half space configuration to simulate the traction free surface of the Earth at the time of faulting.

(Fig. 5). The presence of a number of faults, which are smaller than faults A and B (see Fig. 5a), appears to affect the slip distribution approaching the north tip of fault A and the southwest tip of fault B, producing relatively high slip gradients and smaller perturbations (see Fig. 5c). Therefore, computed and observed slip have to be compared with caution. Despite these com-

plicating factors, the computed slip distributions for the three models are similar in form and symmetry to the observed slip distributions (Fig. 7a and b), especially close to the intersection where we focus our attention. The largest slip on fault A is to the north of the intersection with fault B. The slip decreases significantly toward the south from the intersection line creating a high slip gradient. These observations are reproduced in all three simplified models.

Model (2) appears to fit the observed slip distribution somewhat better than (1) or (3), so these loading conditions were used to compute a contour map of the vertical displacement field on a horizontal observation grid through the center of the model (Fig. 6a). Model results (Fig. 7c) can be compared with the structure contour map based on seismic reflection data (Fig. 5a). Areas of relative uplift and subsidence are similar as well as the general trend of the contours. Maximum subsidence and maximum uplift are located near the fault intersection. Differences in the shape of the contours may reflect the presence of smaller faults.

4.2. Sandbox example

This example, taken from a sandbox experiment (Childs et al., 1993), consists of a normal fault with an associated synthetic hanging wall splay (Fig. 8a). The experiment was conducted primarily to study the geometry and kinematics of basin-scale normal faults with an underlying salt layer. The laboratory model was designed to simulate a two-layered system comprising a brittle overburden of carbonate or terrigenous clastic rock above a viscous décollement layer of rock salt or over-pressured shale (Childs et al., 1993). Thus, the lower boundary corresponds to a shear traction-free surface that models the effects of a ductile layer. For that reason, and also because of the syn-sedimentary nature of the faulting, areas of maximum throw occur at or near the interface between the ductile layer and the overlying sediment.

Using the backstripping technique, the throw changes on syn-sedimentary model faults was examined chronologically (Childs et al., 1993). For the purpose of this discussion, two stages in the fault growth process are described: (1) the faults form an overlap or relay zone between two segments (Fig. 8b); and (2) breaching of the overlap by lateral propagation of one of the overlapping fault segments (Fig. 8c). The linkage permitted the formation of a single through-going fault that continued to grow while the hanging wall splay remained less active.

The resulting fault with its associated synthetic splay shows abrupt change in throw across the intersection line with the splay (Fig. 8c). This observed throw gradient is partly due to the different ways in which the throw distribution on the faults has been displayed on

Fig. 8(b) and (c). Nonetheless, we will show that fault interaction, when the two faults become linked, produces a throw variation at the intersection line that tends to increase the final throw gradient.

In order to emphasize the effect of fault interaction on throw distribution when the faults become linked, we modeled this system in two stages (Fig. 9). In map view, the simplified model configuration approximates the fault geometries (Fig. 8b and c). In three-dimensions, the model faults dip 60° toward the south and are composed of quadrilateral segments (Fig. 9). The faults have the same down-dip dimension and are bounded at their base by a traction-free surface to approximate the ductile layer. The linked fault stage 1 differs from the overlapping stage 2 by the addition of a fault segment between the two faults (Fig. 9b).

Both models have been loaded with a horizontal remote tensile stress of 1 MPa trending perpendicular to the average fault trend. This produces an extension

similar to that imposed in the sandbox. The model assumptions imply that the development of the faults is divided into two distinct slip events and do not explicitly include fault growth except at the fault junction by the addition of a segment to link the faults. Also, a complete stress relaxation at the end of the first event is assumed.

Fig. 10(a) and (b) show the computed throw distribution for the two distinct events, and Fig. 10(c) is the total throw (stage 1 + 2). Computed slip has been converted into throw for comparison with the sandbox example. Observed throw has been used as a reference, so the computed throw distributions have been re-scaled to the maximum observed throw. The computed throw distributions are similar in form to those observed in the sandbox model (Fig. 8b and c). However a significant difference is the observed tapered throw toward the fault tip as observed on the bottom figures of Fig. 10(a) and (b). This effect has
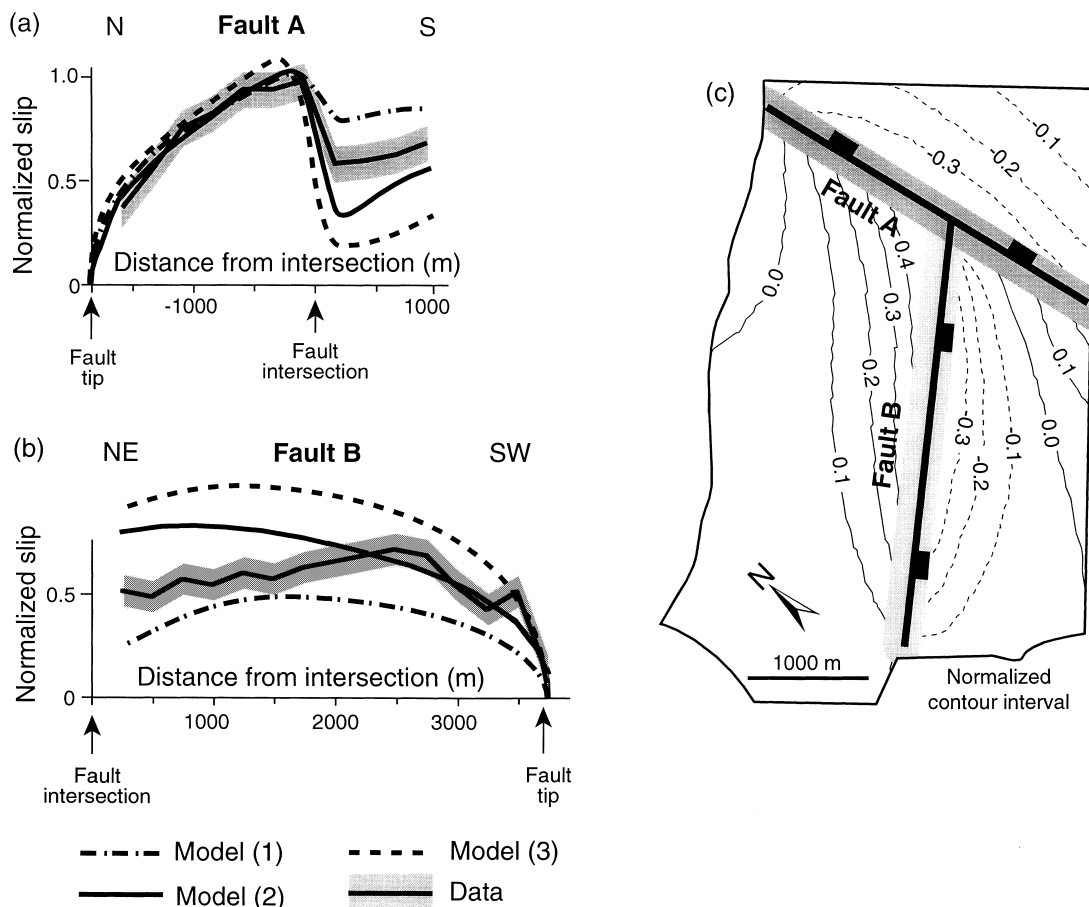

Fig. 7. Computed slip distributions for the North Sea models. (a), (b) Computed slip distributions along horizontal lines through the fault centers, for the three different configurations shown in Fig. 6, compared with the observed slip distribution in Fig. 5. To facilitate the comparison between the observed and the computed slip distribution, the slip has been normalized against the maximum observed slip along fault A. (c) Contours of the normalized computed vertical displacement field, equivalent to a structure contour map, on a horizontal plane through the center of model 2 shown in Fig. 6(b). Gray bands represent areas of no data where observation points are too close to the modeled faults.

been discussed in the earlier section called 'Model assumptions'.

Stage two of the model can be compared to an intermediate stage shown in Fig. 10(b) (dashed line) that represents the throw distribution when the two overlapping sandbox faults became linked. To determine that throw distribution, the throw observed at the base of the faults of the backstripped stage has been sub-

tracted from the throw of the fully developed stage (Fig. 8). We then observe that the splay does not become completely inactive after linkage and that the throw on the main fault is asymmetric with a distinct throw gradient near the intersection line. This stage illustrates the effect of fault interaction immediately after the two segments become physically linked. The computed throw distribution for this stage (Fig. 10b, plain line) is asymmetric, with an enhanced throw on the right-hand side of the major fault relative to the left-hand side. The throw on the minor fault remains less than that on the major fault. These results observed in the data from the sandbox experiments can be explained in terms of fault interaction.

4.3. Conjugate fault example

Simple conjugate normal faults, as observed in seismic sections and in physical models, are commonly composed of faults which dip in opposite directions and either cross at or converge towards an intersection zone (Nicol et al., 1995). The structures are typically X- or Y-shaped in cross-section and the natural examples apparently develop synchronously on a geological time scale. Horsfield (1980), Peacock and Sanderson (1991), Nicol et al. (1995) and Needham et al. (1996) describe some asymmetries in the patterns of
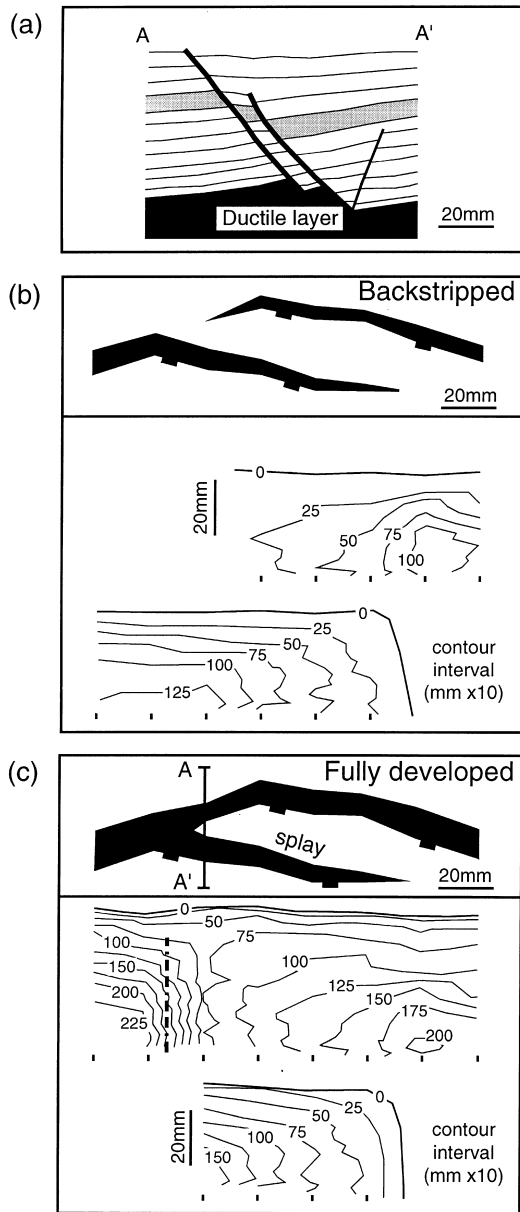

Fig. 8. Intersecting normal faults from sandbox experiment (modified from Childs et al., 1993). (a) Vertical section across the two intersecting faults (bold lines). (b) Geometry of the overlapping faults in plan view associated with their throw distributions. The overlapping geometry represents an early stage of the fault development (obtained by backstripping). (c) Geometry of the intersecting faults in plan view associated with their throw distributions. The intersecting geometry represents the final stage of the fault development.
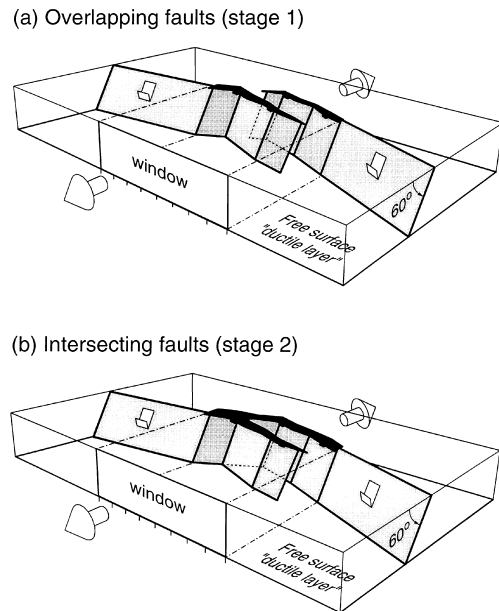

Fig. 9. Model configurations for simulation of the sandbox experiment. The fault geometries have been idealized as shown. Two model configurations have been used to model the sandbox experiment; (a) overlapping fault stage, and (b) the intersecting fault stage. A traction free surface at the base of the faults has been used to simulate the ductile layer. Arrows represent the direction of applied remote tensile stress (1 MPa). The 'windows' represent the position of the numerical results shown in Fig. 10.
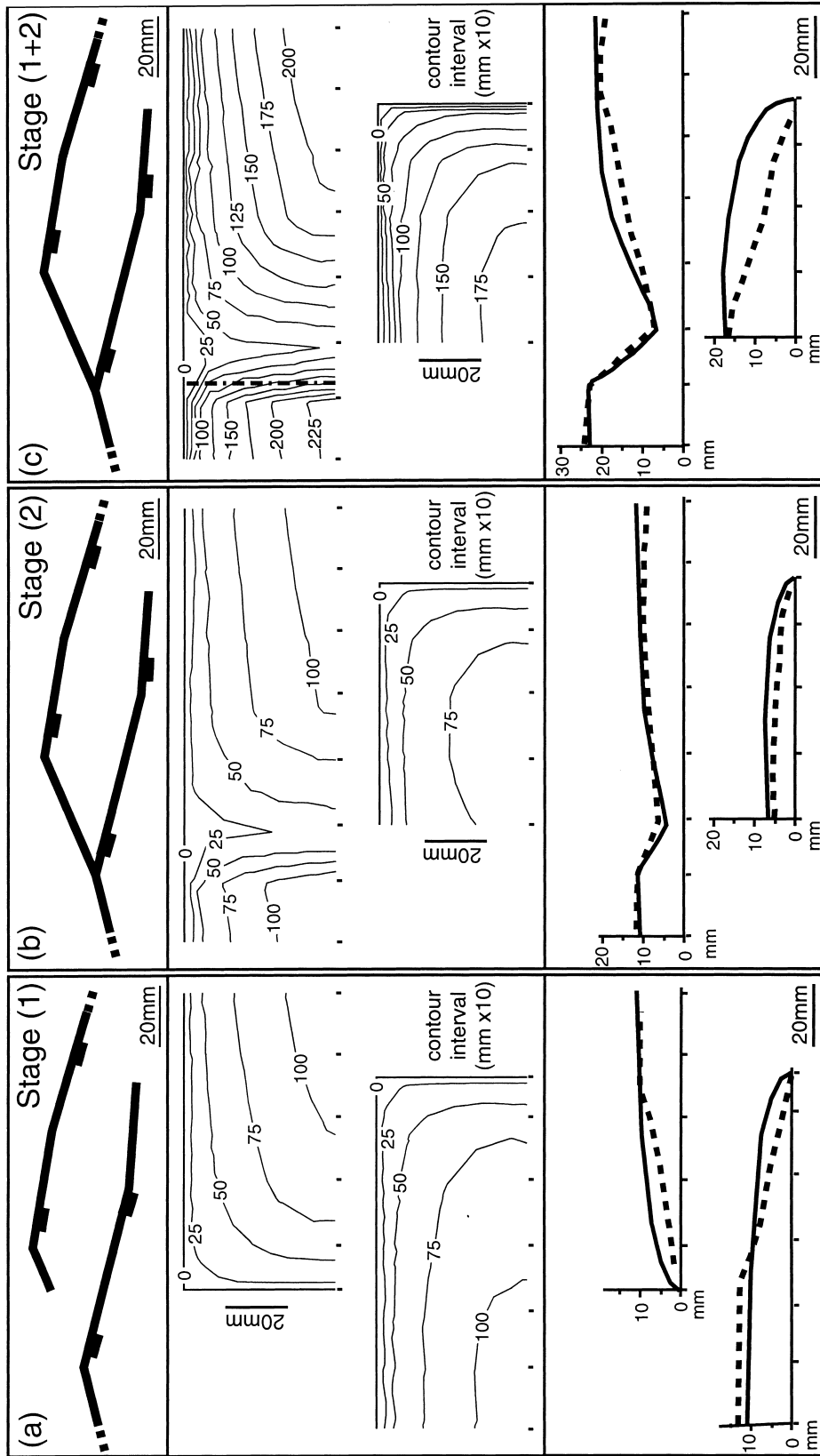
Fig. 10. Model results of sandbox simulation. The computed slip has been converted into throw and normalized against the maximum throw observed in the sandbox to facilitate comparison. (a) Result of the numerical simulation of the overlapping faults (stage 1). The upper figure shows the model configuration in map view. The middle figure shows the computed throw distributions on the two faults. The lower figure shows the throw distributions along a horizontal line through the bottom of the sandbox faults (dashed curves) and the modeled faults (black curves). (b) Result of the numerical simulation of the overlapping faults (stage 2). Dashed curves in the lower figure represent the throw distributions of the fully developed stage (linked fault) minus the throw distribution of the backstripped stage (overlapping fault) along a horizontal line through the bottom of the sandbox faults. (c) Addition of the throw values computed for stage 1 with the throw values computed for stage 2. This corresponds to the fully developed stage of the sandbox experiment. See text for details on the comparison between sandbox example and numerical models.

displacement on fault surfaces that exhibit such conjugate geometry: (1) the slip is reduced toward the intersection line, at which it tends toward zero; and (2) the maximum throw is closer to the intersection line than to the upper tip line. These slip variations seem to be the consequences of interaction between the oppositely dipping faults. An example (Fig. 11) shows the cross-sectional geometry and slip distribution on a fault from the Timor Sea (northern Australia) which is antithetic to a larger fault (Nicol et al., 1996).

To investigate the effect of mechanical interaction on conjugate faults, we used a model geometry as shown in Fig. 12, consisting of a complete circular fault (fault A) and a truncated half-circular fault (fault B) forming a Y-shaped system. The two faults are linked along their horizontal axes and dip in opposite directions to form a 60° angle between the faults. This conjugate system was embedded in a whole elastic space and was loaded remotely by a vertical compression ($\sigma_{zz} = -1$ MPa).

Fig. 13 summarizes the results, showing computed slip contours on both faults and the slip distribution along a vertical line through the center of each fault. The fault slip is normalized to the maximum elliptical slip that would occur on an isolated fault (dashed lines). The computed slip on the antithetic fault B shows a reduced value (close to zero) near the intersection line and a maximum slip not adjacent to the intersection line, as observed in Fig. 11(b). Fault A exhibits an increasing slip upward and decreasing downward with a maximum just above the line of intersection.

The model results show that asymmetric slip distributions and maximum slip away from the intersection line on the antithetic fault do not necessarily mean that nucleation of the faults occurred at some distance from the intersection line (Nicol et al., 1995, 1996). Our results do not deny this possibility, but show that the asymmetric maximum slip can be due simply to mechanical interaction between conjugate faults that could have nucleated and grown from the same location within the intersection zone. Clearly some independent information (other than slip) is needed to distinguish these two mechanisms.

5. Conclusions

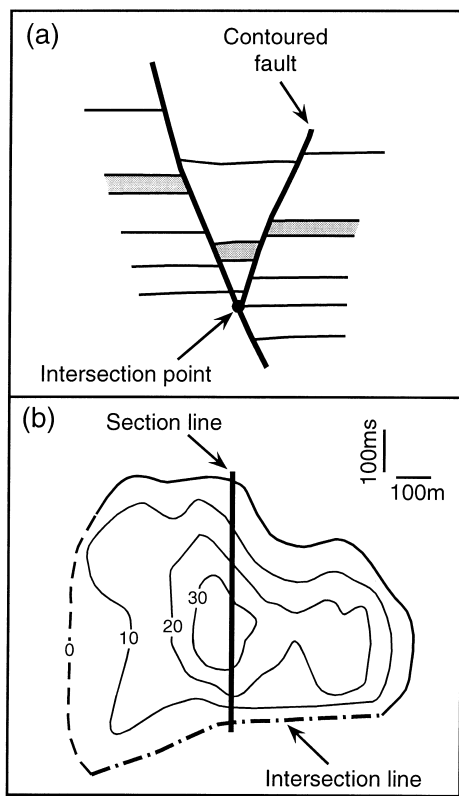The present study documents mechanical relationships between three-dimensional fault geometry and

Fig. 11. Conjugate normal faults from the Timor Sea (modified from Nicol et al., 1996). (a) Cross-section showing the Y-shaped geometry of a normal fault and a smaller antithetic fault. The location of the cross-section is shown on (b). (b) Throw contour diagram (in ms) of the antithetic fault viewed normal to the fault surface. The fault is antithetic to the larger fault, which intersects at an intersection line; an intersection point in cross-section is shown in (a). The slip distribution terminates downwards at the intersection line where it tends to zero, whereas the maximum throw is located centrally.
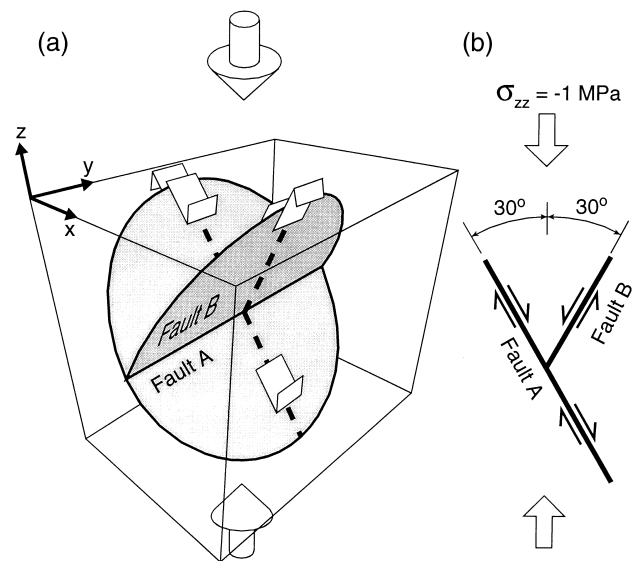

Fig. 12. Model configuration for simulation of conjugate faults. (a) Three-dimensional view of the model. The faults are circular (1 unit radius) and half circular, and are linked by a horizontal intersection line. Dashed lines are the observation lines of Fig. 13(b). (b) Cross-section of the model through the observation lines. The faults dip 60° in opposite directions to form a 60° angle between the conjugates. The faults are embedded in an elastic whole space and are loaded remotely by a vertical compressive stress (−1 MPa).
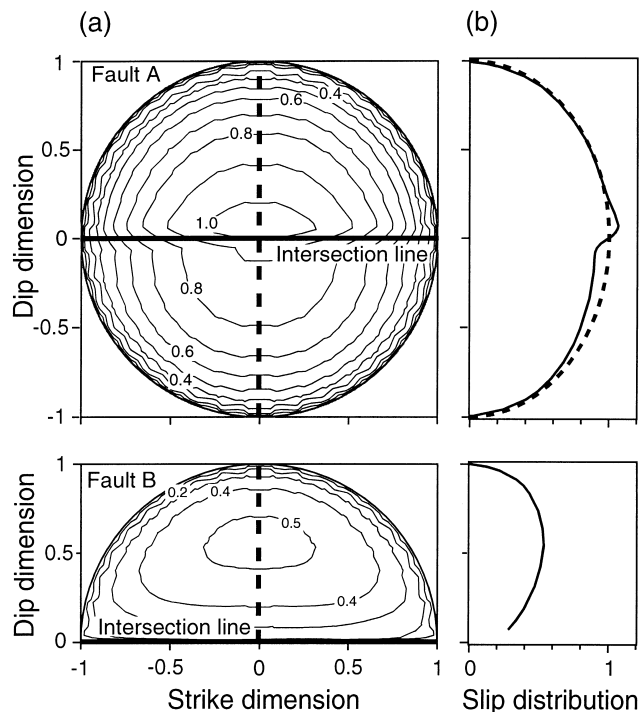
Fig. 13. Computed fault slip distributions for the conjugate fault model. (a) Contours of normalized slip along the two conjugates. The contour value of 1 indicates the maximum that would occur on a single isolated fault. Dashed vertical lines are the position of (b). (b) Slip distribution on the faults along a vertical line through their center. The plain curve shows the normalized computed slip distribution and the dashed curve represents slip along a single circular isolated fault. The antithetic fault shows its maximum slip centrally and its slip distribution tending toward zero close to the intersection line, as shown on the Timor Sea fault example (Fig. 12).

slip distribution. We have shown that elastic deformation between faults that are arranged in complex arrays, such as intersecting faults, produces slip distributions that are similar to observed slip distributions. The following conclusions can be drawn from the correspondence between previous observations and our numerical analysis:

1. When one fault links to another, the intersected fault is divided by the line of intersection and develops two asymmetric slip maxima, one on either side of the intersection line.
2. The large slip gradients and asymmetries in patterns of slip contours observed near intersection lines can be caused by mechanical interaction between the faults. This interaction is attributed, at least in part, to elastic deformation that modifies the local shear stress acting on one fault as induced by slip on the other fault.
3. Variation in the strike angle between branched faults has a strong effect on fault interaction and thus on the slip distribution. For some geometries the slip can be greater than would occur on an iso-

lated fault. On the other hand, the slip can be sensibly reduced relative to the isolated fault for other geometries.
4. In spite of considerable simplifications in geometry and boundary conditions to facilitate the numerical models, the computed slip distributions capture many of the slip characteristics observed in nature and laboratory sandbox experiments.

Of course the correspondence between the results of our numerical analyses and observations is not perfect because many factors have not been considered in our idealized models. Examples include the three-dimensional nature of the tectonic stress field, temporal changes in the tectonic stress field, spatial variation of material properties, fault growth, inelastic deformation, friction on the fault plane, etc. Nevertheless, many complexities in natural slip distributions can be understood using relatively simple mechanical models (Willemse et al., 1996).

References

Anderson, E.M., 1951. The Dynamics of Faulting. Oliver & Boyd, London.

Aydin, A., Reches, Z., 1982. Number and orientation of fault sets in the field and in experiments. Geology 10, 107–112.

Barnett, J.A.M., Rippon, J.H., Walsh, J.J., Watterson, J., 1987. Displacement geometry in the volume containing a single normal fault. American Association of Petroleum Geologists Bulletin 71, 925–937.

Becker, A.A., 1992. The Boundary Element Method in Engineering. McGraw-Hill, New York.

Brewer, J.A., Smythe, D.K., 1984. MOIST and the continuity of crustal reflector geometry along the Caledonian–Appalachian orogen. Journal of Geological Society, London 141, 105–120.

Bürgmann, R., Pollard, D.D., Martel, S.J., 1994. Slip distributions on faults: effects of stress gradients, inelastic deformation, heterogeneous host-rock stiffness, and fault interaction. Journal of Structural Geology 16, 1675–1690.

Childs, C., Easton, S.J., Vendeville, B.C., Jackson, M.P.A., Lin, S.T., Walsh, J.J., Watterson, J., 1993. Kinematic analysis of faults in a physical model of growth faulting above a viscous salt analogue. Tectonophysics 228, 313–329.

Childs, C., Watterson, J., Walsh, J.J., 1995. Fault overlap zones within developing normal fault systems. Journal of Geological Society, London 152, 535–549.

Clark Jr, S.P. (Ed.), 1966. Handbook of Physical Constants, revised ed. Geological Society of America, Memoir 97.

Cohen, S.C., 1984. Postseismic deformation due to subcrustal viscoelastic relaxation following dip-slip earthquakes. Journal of Geophysical Research 89, 4538–4544.

Comminou, M., Dunders, J., 1975. The angular dislocation in a half-space. Journal of Elasticity 5, 203–216.

Coward, M.P., Enfield, M.A., 1987. The structure of the West Orkney and adjacent basins. In: Brook, J., Glennie, K. (Eds.), Petroleum Geology of North West Europe, 3rd Conference on Petroleum Geology of North West Europe Proceedings, pp. 687–696.

Cowie, P.A., Scholz, C.H., 1992. Physical explanation for the displacement–length relationship of faults using a post-yield fracture mechanics model. Journal of Structural Geology 14, 1133–1148.

Cowie, P.A., Shipton, Z.K., 1998. Fault tip displacement gradients and process zone dimensions. Journal of Structural Geology 20, 983–997.

Crouch, S.L., Starfield, A.M., 1983. Boundary Element Methods in Solid Mechanics: with Applications in Rock Mechanics and Geological Engineering. Allen & Unwin, Winchester, Massachusetts.

Enfield, M.A., Coward, M.P., 1987. The structure of the West Orkney Basin, northern Scotland. Journal of Geological Society, London 144, 871–884.

Fernandez, J., Yu, T.-T., Rundle, J.B., 1996. Horizontal viscoelastic-gravitational displacement due to a rectangular dipping thrust fault in a layered Earth model. Journal of Geophysical Research, B, Solid Earth and Planets 101, 13581–13594.

Fossen, H., Rørnes, A., 1996. Properties of fault populations in the Gullfaks Field, northern North Sea. Journal of Structural Geology 18, 179–190.

Horsfield, W.T., 1980. Contemporaneous movement along crossing conjugate normal faults. Journal of Structural Geology 2, 305–310.

Jeyakumaran, M., Rudnicki, J.W., Keer, L.M., 1992. Modeling slip zones with triangular dislocation elements. Seismological Society of America Bulletin 82, 2153–2169.

Krantz, R.W., 1988. Multiple fault sets and three-dimensional strain: theory and application. Journal of Structural Geology 10, 225–237.

McClay, K.R., Norton, K.R., Coney, P., Davis, G.H., 1986. Collapse of the Caledonian orogen and the Old Red Sandstone. Nature 323, 147–149.

Maerten, L., 1998. Inferring fault linkage from seismic data and numerical analysis: application to the Oseberg Syd reservoir compartmentalization (abstract). American Association of Petroleum Geologists 1998 annual convention, Salt Lake City.

Needham, D.T., Yielding, G., Freeman, B., 1996. Analysis of fault geometry and displacement patterns. In: Buchanan, P.G., Nieuwland, D.A. (Eds.), Modern Development in Structural Interpretation, Validation and Modelling. Special Publication of the Geological Society, London 99, pp. 189–199.

Nicol, A., Walsh, J.J., Watterson, J., Bretan, P.G., 1995. Three-dimensional geometry and growth of conjugate normal faults. Journal of Structural Geology 17, 847–862.

Nicol, A., Watterson, J., Walsh, J.J., Childs, C., 1996. The shapes, major axis orientations and displacement patterns of fault surfaces. Journal of Structural Geology 18, 235–248.

Oreskes, N., Shrader-Frechette, K., Belitz, K., 1994. Verification, validation, and confirmation of numerical models in the Earth Sciences. Science 263, 641–646.

Peacock, D.C.P., Sanderson, D.J., 1991. Displacements, segment linkage and relay ramps in normal fault zones. Journal of Structural Geology 13, 721–733.

Peacock, D.C.P., Sanderson, D.J., 1994. Geometry and development of relay ramps in normal fault systems. American Association of Petroleum Geologists Bulletin 78, 147–165.

Peacock, D.C.P., Sanderson, D.J., 1996. Effects of propagation rate on displacement variations along faults. Journal of Structural Geology 18, 311–320.

Reches, Z., 1987. Determination of the tectonic stress tensor from slip along faults that obey the Coulomb yield condition. Tectonics 6, 849–861.

Rippon, J.H., 1985. Contoured patterns of throw and hade of normal faults in the coal measures (Westphalian) of northeast Derbyshire. Proceedings of the Yorkshire Geological Society 45, 147–161.

Roberts, A.M., Badley, M.E., Price, J.D., Huck, I.W., 1990. The structural history of a transtensional basin: Inner Moray Firth, NE Scotland. Journal of Geological Society, London 147, 87–103.

Rundle, J.B., 1982. Viscoelastic-gravitational deformation by a rectangular thrust fault in a layered Earth. Journal of Geophysical Research 87, 7787–7796.

Sih, G.C., 1975. Three-dimensional Crack Problems. Noordhoff International, Leiden.

Tada, H., Paris, P.C., Irwin, G.R., 1985. The Stress Analysis of Cracks Handbook. Paris Productions Incorporated, St. Louis.

Thomas, A.L., 1993. Poly3D: a three-dimensional, polygonal-element, displacement discontinuity boundary element computer program with applications to fractures, faults, and cavities in the Earth's crust. M.S. thesis, Stanford University, California.

Walsh, J.J., Watterson, J., 1987. Distribution of cumulative displacement and seismic slip on a single normal fault. Journal of Structural Geology 9, 1039–1046.

Walsh, J.J., Watterson, J., 1989. Displacement gradients on fault surfaces. Journal of Structural Geology 11, 307–316.

Walsh, J.J., Watterson, J., 1991. Geometric and kinematic coherence and scale effects in normal fault systems. In: Roberts, A.M., Yielding, G., Freeman, B. (Eds.), The Geometry of Normal Faults. Special Publication of the Geological Society, London 56, pp. 193–203.

Watterson, J., 1986. Fault dimensions, displacements and growth. Pure and Applied Geophysics 124, 365–373.

Willemse, J.M., 1997. Segmented normal faults: correspondence between three-dimensional mechanical models and field data. Journal of Geophysical Research 102, 675–692.

Willemse, J.M., Pollard, D.D., Aydin, A., 1996. Three-dimensional analyses of slip distribution on normal fault arrays with consequences for fault scaling. Journal of Structural Geology 18, 295–309.